



An efficient and unique route for the fabrication of highly condensed oxygen-doped carbon nitride for the photodegradation of synchronous pollutants and H₂O₂ production under ambient conditions

Milad Jourshabani, Mahdieh Razi Asrami, Byeong-Kyu Lee^{*}

Department of Civil and Environment Engineering, University of Ulsan, Daehakro 93, Namgu, Ulsan 680-749, Republic of Korea

ARTICLE INFO

Keywords:

Supramolecular self-assembly
Anion doping
Carbon nitride
Photodegradation
H₂O₂ production

ABSTRACT

N₂-assisted thermal polycondensation of a novel supramolecular self-assembly based on melamine, cyanuric acid, and thiourea produced S-doped carbon nitride. Molecular dynamics simulation estimated nonbonding energies between the melamine-cyanuric acid adduct and thiourea. The C–S functional group was efficiently converted to C–O by facile calcination in a static air atmosphere, which gave a highly condensed O-doped carbon nitride nanosheet (O-CN). Density functional theory (DFT) calculations and experimental results confirmed that the oxygen-doped site is more stable and provides midgap states near the conduction band position of CN compared with sulfur doping. O-CN exhibited excellent visible light harvesting and photocatalytic activities toward removal of tetracycline and rhodamine B in an initial 15 min while producing a highly stable amount of H₂O₂ under an open atmosphere without a sacrificial agent. These outstanding performances result from synergistic approaches that lead to the modified polycondensation process, unprecedented reduction ability, and enhanced optical properties.

1. Introduction

The presence of hazardous and nonbiodegradable organic compounds on waterways has raised great concern [1,2]. In addition, pharmaceuticals and personal care products have been well reported to pass through wastewater treatment plants, posing a potential risk to ecosystems and human health [3]. For example, tetracycline (TC), the second most frequent antibiotic in human and animal therapy, has been considered an emerging non-easily degradable organic compound discharged from municipal sewage [4]. Therefore, traditional methods that include absorption, aerobic/anaerobic microbial degradation, and liquid membrane suffer from shortcomings such as secondary product generation, incomplete degradation, and costly and time-consuming processes [5]. However, the implementation of complementary techniques such as UV/hydrogen peroxide (H₂O₂), as an advanced oxidation process, has been used in wastewater treatment plants as a pretreatment step for refractory wastewater to provide readily biodegradable feed wastewater for microbial treatment [6]. H₂O₂ is a highly efficient and environmentally benign oxidant without toxic side reactions in an aqueous environment. Therefore, it has been frequently applied in wastewater treatment and disinfection, and its lifetime ensures stable

disinfection in the waterbody.

Currently, visible light photocatalysis technology is an effective and promising way to degrade a wide range of stubborn organic contaminants in wastewater. Meanwhile, photocatalytic production of H₂O₂ has recently attracted much interest due to its green, cost-effective and safe method compared to the industrial anthraquinone process [7]. However, using the alcoholic solution as a sacrificial agent and blowing oxygen gas [8] would not be favorable to the production of H₂O₂ and the photodegradation of organic contaminants since it would increase capital and operating costs for implementation.

Polymeric carbon nitride (CN) has shown noticeable activities for the photocatalytic removal of pharmaceuticals [9,10] and also the synthesis of H₂O₂ by blowing O₂ and the use of sacrificial agents [7]. This material is a low-cost, simple, and metal-free photocatalyst with a visible light response. Only a handful of semiconductors such as CN overcome the thermodynamic barriers for •O₂[−] half-reaction, which originate from its more negative levels of conduction band CB [11,12]. Nevertheless, the solid-state polymerization of starting materials gives a partial crystalline and bulk character to the CN, which has a low surface area and photocatalytic active sites, and consequently, less performance. In this sense, melamine (ML) as the main constituent of a building block in the

^{*} Corresponding author.

E-mail address: bklee@ulsan.ac.kr (B.-K. Lee).

<https://doi.org/10.1016/j.apcatb.2021.120839>

Received 3 August 2021; Received in revised form 5 October 2021; Accepted 19 October 2021

Available online 23 October 2021

0926-3373/© 2021 Elsevier B.V. All rights reserved.

intermediate CN tends to be sublimated during the polycondensation process. The molecular self-assembly of melamine with other triazine derivatives addresses the problem to some extent and forms a new starting material with different physical properties [13–15]. Hence, supramolecular preassembly as a cheap, easily accessible, and scalable approach has become more significant to deal with the shortcomings of bulk CN. For example, a complex of cyanuric acid plus melamine (CM) was reported in a dimethylsulfoxide (DMSO) solvent, and the resultant CN removed the rhodamine B (RhB) solution (10 mg L^{-1}) after 105 min [14].

Nevertheless, one single modification hardly boosts the photocatalytic performance of metal-free CN to a great level, and a further improving approach needs to be considered. Among other modification methods, nonmetal doping, such as oxygen and sulfur, further tunes optical properties by narrowing the band gap, tailoring electronic structures, and creating an absorption tail in visible and near-infrared regions [16]. For example, Li et al. synthesized bulk O-doped CN using a hydrothermal approach in the presence of H_2O_2 as a strong oxidant. However, O-doped CN showed an extended absorbance edge up to 498 nm, a high surface area, and impressive charge separation; it still had bulk morphology with a low condensed structure [17].

Interestingly, thiourea has become a multifunctional material. It acts as a precursor for the synthesis of CN as does sulfur doping in CN [18]. It is even more interesting as a template for orienting specific molecules in the solid-state [19]. Inspired by the above facts and intriguing characteristics of thiourea, we found that the presence of thiourea not only act as sulfur doping function, but also can pave a regular directionality to the supramolecular precursor. What is more, the sulfur site can be replaced by oxygen doping under static air atmosphere during annealing process.

Herein, a supramolecular complex with a regular hexagonal morphology was prepared via hydrogen bonding between melamine, cyanuric acid, and thiourea (MCT) in water as the green solvent. Thiourea (TU), in turn, holds subunits of the hexagonal cyanuric acid-melamine face through nonbonding interactions in a well-organized direction, as discussed by molecular dynamics simulations for the first time. Metal-free S-doped CN (S-CN) was obtained by thermal polycondensation of MCT under a nitrogen atmosphere. Afterwards, the sulfur-doped sites in S-CN were efficiently converted to C-O by simple calcination under a static air atmosphere without any additive. Density functional theory (DFT) calculations and experimental results confirmed that the oxygen-doped site is more stable and gives midgap states near the CB position than sulfur doping. The resulting ultrathin O-doped CN nanosheet shows superb visible light photodegradation of TC and RhB within an initial 15 min while producing highly stable production of H_2O_2 as much as $168.1 \mu\text{mol g}^{-1} \text{ h}^{-1}$ under ambient atmosphere without a sacrificial agent. Moreover, TC intermediates, their toxicities, and possible photocatalytic mechanism were discussed in detail.

2. Experimental section

The Chemicals, Computational details, Characterization, Electrochemical measurements, Photocatalytic activity tests and Identifying active species parts are presented in the [Supporting Information](#).

2.1. Preparation of supramolecular based on ML, CY, and TU (MCT)

Since the ratio of precursor molecules has shown substantial effects on the self-assembled supramolecular shape, the mass ratios of TU to ML:CY (3:3) were optimized comprehensively in this study. In a typical synthesis, 3.0 g ML, 3.0 g CY, and 3.0 g TU were separately added to 40 mL of the boiling water. After stirring for 30 min, each solution was quickly transferred to Teflon-lined autoclave reactors under stirring for 30 min. The autoclave was sealed in the oven at 100°C for 4 h and then naturally cooled. The suspension was then centrifuged and dried at 80°C in the oven overnight. Finally, the dried solids were ground to a white

powder and named MCT (M, C, T), where M, C, and T were the mass content of melamine, cyanuric acid, and thiourea. To feel reassured, we also synthesized a sample of CM supramolecular at the same conditions as MCT without TU to investigate the role of TU on the photo-degradation performance.

2.2. Preparation of CN

Solids from the previous step were loaded into lid-loaded crucibles and calcined at 540°C for 4 h in a nitrogen atmosphere with a heating rate of $2.5^\circ\text{C min}^{-1}$. The prepared S-doped CN with the best mass ratio, denoted as S-CN (3, 3, 3), was further thermally treated at 540°C for 3 h in a static air atmosphere with a heating rate of $2.5^\circ\text{C min}^{-1}$. The resulting O-doped CN is named O-CN. To investigate the effect of morphology and other characteristics on the product, control samples were also synthesized by pyrolysis of thiourea (CN-TU) and melamine (CN-ML) as starting materials at 540°C for 3 h under air atmosphere. For further comparison, a sample of CN was also prepared by calcination of a common CM complex (CN-CM) under the same conditions as those for S-CN.

3. Results and discussion

3.1. Chemical structure and morphology of MCT

The supramolecular aggregates are obtained by different mass ratios of TU, ML, and CY in water. Fig. 1 shows the effect of various mass ratios of TU on the morphology of the MCT. As seen, the MCT (3, 3, 1.32) that has the lowest TU content exhibits irregular and bulk morphology (Fig. 1a). After increasing the amount of TU to 3 g, the hexagonal morphology with the six-sided face is separated from the solution, suggesting that the presence of TU molecules provides regular orientations for other members (Fig. 1b). Interestingly, by increasing the TU content to 4.68 g, the hexagonal face grows longitudinally to create a hexagonal prismatic structure with a six-sided face (Fig. 1c). The TEM image of the optimized MCT (3, 3, 3) discloses that the regular arrangement of a rod-like structure is dominant throughout the supramolecular structure (Fig. 1e and f). Furthermore, the EDX mapping clearly shows the rod-like structure of MCT (3, 3, 3) and the homogeneous distribution of C, N, and O atoms within the particle (Fig. 1g), indicating that the S atom is dispersed along the stacking axis. In addition, the effect of various mass ratios of ML and CY on the final MCT structure is also investigated by SEM images (Fig. S1). Moreover, it is well documented that protic and aprotic solvents, such as water, ethanol, dimethyl sulfoxide, and chloroform result in various directionalities of noncovalent bonds. Hence, the solvent effect of DMSO on the sample MCT (3, 3, 3) was investigated as shown in Fig. S1e, revealing an irregular plate-like structure. Therefore, the following characterizations focus mainly on the optimized supramolecular structure, i.e., MCT (3, 3, 3) in water.

As shown in Fig. 2a, the molecular structure of the optimized MCT was further assessed by TGA and DSC techniques. Around 4.1% of mass loss is observed at an initial 173°C , which is confirmed by a small endothermic peak in the DSC curve. This might arise from the evaporation of crystal water amount or rearranging precursors and releasing gas, followed by a step-change temperature at 237°C in the DSC. Interestingly, a significant heat flow is released at 272°C with a sharp exothermic peak. This indicates a high degree of crystallization, leading to the thermal resistance of up to 320°C for the MCT sample. Furthermore, there is no DSC peak in the cooling process, indicating that after 400°C , the material is completely volatilized. Finally, it is noteworthy that the mass loss of pure melamine starts at 245°C (Fig. S2). This result shows that the new supramolecular structure remarkably retards the sublimation of intermediates and helps the polycondensation process in solid-state reactions.

The optimized MCT XRD pattern exhibits new crystallinity, which is

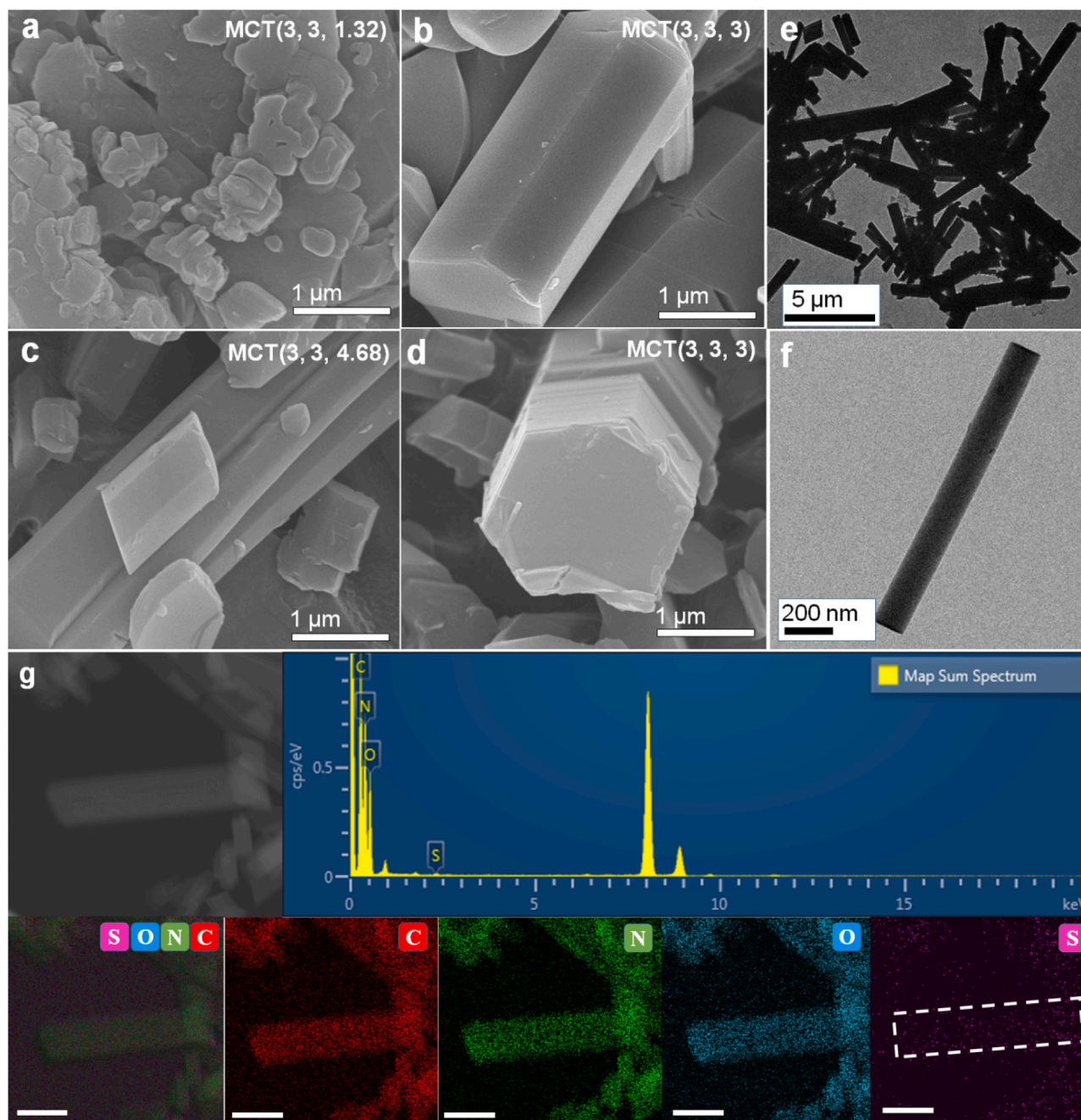


Fig. 1. SEM images supramolecular with different TU contents (a) MCT (3, 3, 1.32), (b) MCT (3, 3, 3), (c) MCT (3, 3, 4.68), and (d) six-sided face of MCT (3, 3, 3); (e) low- and (f) high-magnification TEM images of the optimized MCT (3, 3, 3); (g) High-angle annular dark-field scanning TEM and EDX mapping images of C, N, O, and S atoms. Scale bars: 1 μm .

confirmed by the presence of new and prominent peaks at around 10.8, 11.8, 21.9, 28.1, and 33.2° (Fig. 2b). Close inspection of Fig. 2b shows that all pivotal diffraction patterns of ML, CY, and TU have disappeared in the reborn MCT structure, indicating the successful self-assembly and new orientation of the ML, CY, and TU monomers. Guo et al. presented simulated patterns of the well-known supramolecular assembly of CM in which ML and CY are held together by hydrogen bonds and the effect of phosphorus, endowing rod-shaped shape in a perpendicular direction by π - π interaction. They predicted three strong diffraction peaks at around 11, 12, and 28° for this structure [20]. Here, the XRD patterns of the optimized MCT are completely consistent with the simulated results, which means that the ML and CY molecules still have a strong chemical affinity with three hydrogen bonds. It suggests that the TU molecules

cannot interrupt this strong affinity. Notably, with further consideration of the XRD patterns of MCT, no obvious peaks associated with unreacted TU are observed.

The optimized MCT sample indicates a prominent difference in the FT-IR spectrum compared to the bare CY, ML, and TU, resulting from the formation of hydrogen bonds between them (Fig. 2c). New and more prominent peaks appear in the 1357–1813 cm^{-1} region, confirming the new interactions within the MCT complex. It is also well documented that CY molecules are connected to ML molecules through the hydrogen bonds of N-H...O and N-H...N, and this causes a positive shift of the vibration frequency in CY and a negative of the vibrations of the triazine ring in ML [13]. In our case, the C = O peak is shifted from 1692 to 1735 cm^{-1} , while N-H shows a peak shift of 812–764 cm^{-1} .

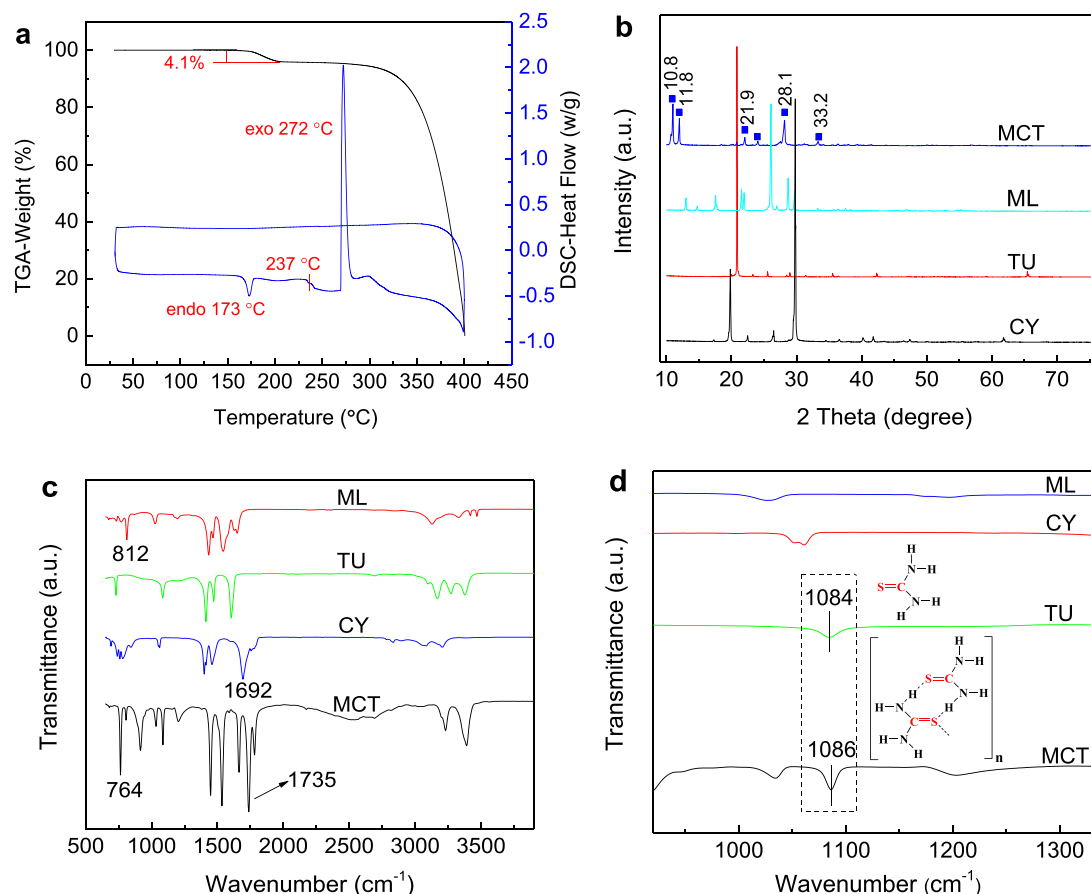


Fig. 2. (a) TGA and DSC of the optimized MCT; (b) XRD patterns, (c) FT-IR, and (d) the magnified FT-IR of the sulfur region of the optimized MCT along with control samples.

The SEM, XRD, and FTIR results strengthen the assumption that TU does not rupture the traditional supramolecular assembly of CM. Instead, TU might provide a template to orient the crystal growth of the CM assembly. Recently, X-ray crystallographic studies have explored the potential of TU as a template for reorganizing various molecules, in which TU molecules may form infinite tapes through hydrogen bonds [21]. To confirm the presence of TU in the MCT, XPS measurements were also used (Fig. S3). A wide symmetry peak is observed at around 163.5 eV, which can be evident in the TU components in MCT. Lindberg et al. comprehensively investigated the electron bonding energy of sulfur atoms in aliphatic sulfur compounds and showed that the binding energy of (S₂)C=S appeared at 163.4 eV [22]. Therefore, the peak at around 163.5 eV is probably attributable to the presence of TU instead of sulfur doping in the aromatic ring of supramolecular texture. Furthermore, the presence of sulfur in the supramolecular assembly is also confirmed by elemental analysis (0.17 wt%), which is close to the sulfur obtained from the EDX result (0.21 wt%). It is suggested that TU is not the main building block of the adduct and might be located between the high-order hexagonal faces as template molecules. The ability of TU to preorient different types of organic molecules in the crystalline state has been well explored. Ramamurthy et al. extensively used TU as a co-crystal to guide olefins in the crystalline state [21]. This might not be surprising since TU might form zigzag or linear tapes through the N-H...S bond, which holds the 2D face of supramolecular molecules by free nonbinding interactions.

A magnified view of the FT-IR results belonging to the sulfur region is shown in Fig. 2d. As shown, the solid-state of the TU molecules shows a stretching vibration of C=S at 1084 cm⁻¹, while there is no similar peak for ML or CY in this region [23]. More interestingly, the C=S peak becomes more pronounced and shows a slight shift to a higher

frequency, which is reasonable considering the higher sulfur content and noncovalent interactions of thiourea with each other via N-H...S in the new orientation. In particular, the short movement in frequency is predictable since the electronegativities of sulfur (2.58) and hydrogen (2.20) are close together within intermolecular interaction. It should also be noted that the N-H...O interactions are stronger than the N-H...S. Furthermore, the ML and CY molecules have similar conformations and spatial orientations, so they quickly react with each other via hydrogen bonding. According to control experiments, as soon as the ML solution was added to the CY solution, the white precipitation formed rapidly, while mixing the TU solution with the ML or CY solutions did not give such precipitation (Fig. S4). Nevertheless, adding TU to either ML or CY solutions led to the precipitation of crystal particles after a long time, manifesting the kinetic trend of TU molecules to interact with counterparts.

As a result, TU might first form hydrogen bonding (N-H...S) and then organize the CM supramolecular assembly into higher-order assemblies of hexagonal shape. If so, it is anticipated that the different hydrogen bond patterns are involved between the TU tapes and the CM self-assembly. To ascertain this, molecular dynamics simulations were carried out to estimate the preferred position of hydrogen bonding and the type of atom in CM self-assemblies, O or N (Fig. 3). Hence, the hydrogen bonding energy of each position was calculated to obtain better insight into the intermolecular interactions. Comparing the non-binding energies ($\Delta E_{\text{non-binding}}$) of the (A) - (D) structures, some important clues would suggest: (i) TU with zigzag tape shows more negative $\Delta E_{\text{non-binding}}$ than linear tape via the N-H...O linkage. This result is consistent with previous reports in which the TU zigzag tape was applied to orient olefins in parallel arrangement [21], and (ii) at the atomic scale, the intermolecular interaction of N-H...N is more prone than that for the

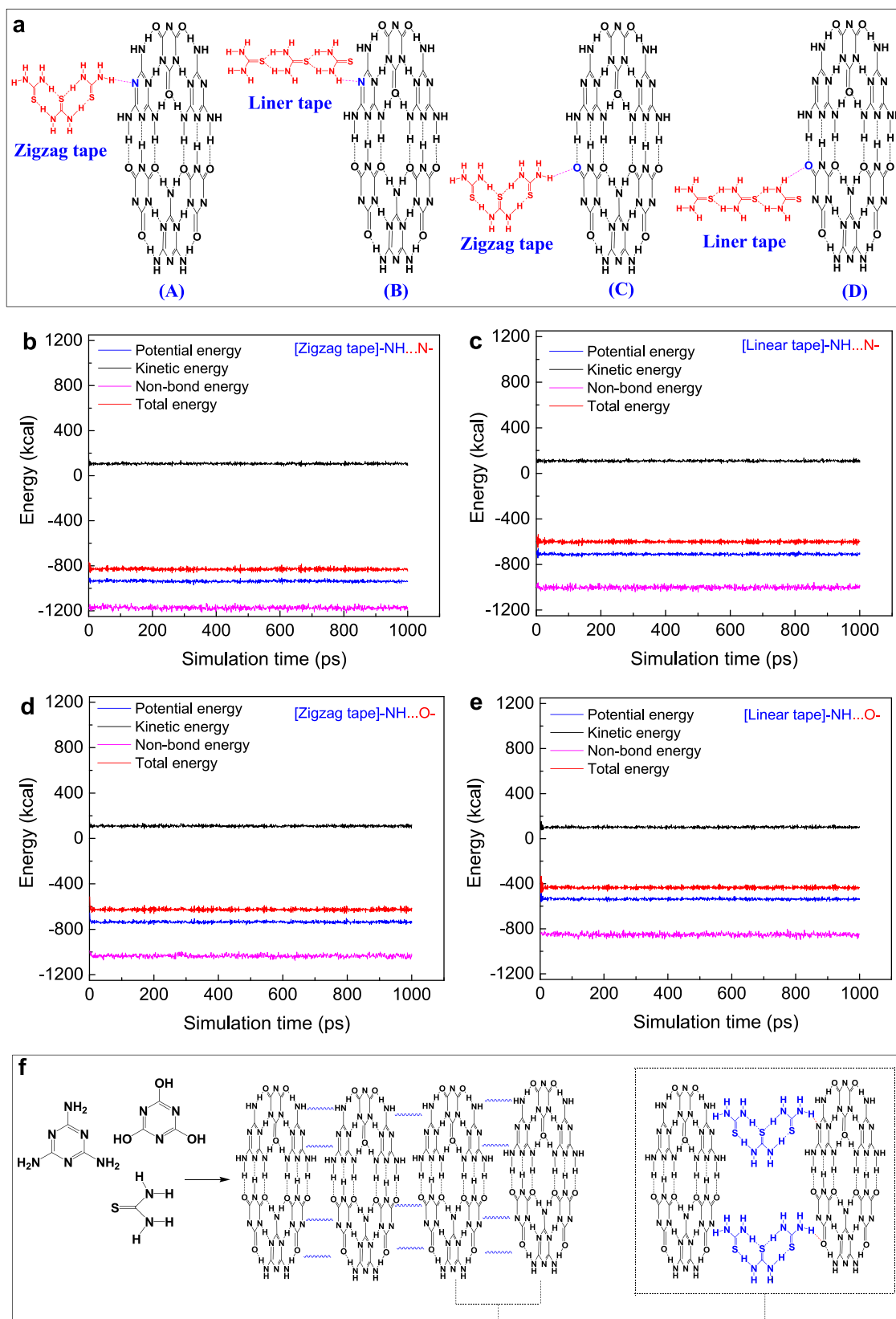


Fig. 3. (a) The proposed positions in which TU with different synthons can steer the CM complex via hydrogen bonds on the N or O sites and hold them in a regular arrangement; (b,c,d,e) Nonbonding energies of systems in which TU with different synthons can form hydrogen bonds on the N or O sites; (f) Schematic formation of the MCT complex.

N-H...O linkage, since the former releases more energy.

3.2. Pyrolysis of MCT to S-CN and O-CN

3.2.1. Chemical structure and morphology of CNs

MCTs with different ML, CY and TU amounts were converted to CN by thermal polycondensation at 540 °C for 3 h under a nitrogen atmosphere (S-CN). SEM images of CN with the lowest mass of TU show homogeneous coral-like morphologies (Fig. 4a), while in the case of optimized S-CN (3, 3, 3), CN grows in two directions, like sprouts inside an exoskeleton network (Fig. 4b). With an increase in the TU content to 4.68 g, a large sheet-like morphology with some sprouting on the surfaces is observed. The sheet-like pieces might be due to the rupture of the original hexagonal faces of the complex during thermal polycondensation (Fig. 4c). Note that the nonbonding interactions cannot be retained at high temperatures. To strengthen this speculation, the optimized supramolecular assembly, that is, MCT (3, 3, 3), was heated at 500 °C for 3 h under a nitrogen atmosphere. As shown in Fig. S5, the hexagonal faces start disappearing, while some sprouting of coral-like morphologies appears. Furthermore, the best self-assembly after thermal treatment under static air atmosphere, i.e., O-CN, includes a nanosheet structure with ordered morphology, indicating more exfoliation (Fig. 4d). The TEM results of S-CN, as well as O-CN, are shown in Fig. 4e and f, respectively. S-CN shows a very weak contrast after encountering electron beams compared with CN-TU and CN-ML (Fig. S6a and b), disclosing a wide improvement in the properties of the carbon nitride and its narrowed thickness. Interestingly, thermal treatment in the presence of air leads to the disappearance of the curling of the nanosheets and flattening of the structure. Therefore, the surface

tension is significantly reduced in the O-CN sample. The AFM results show ultrathin nanosheets of O-CN with an approximate thickness of around 3.5 nm, compared with CN-ML (70 nm) as the reference (Fig. 4g and h). In particular, all the CN architectures obtained in this study are different from the original structure of MCT. The reason is probably that TU not only acts as a template or holder for other molecules but can also itself convert to a CN structure, possibly endowing a new semi-conducting domain.

The FT-IR results demonstrate an improvement in the pyrolysis process, as shown in Fig. 4i. All stretching modes of triazine rings are significantly emerged from 1200 to 1650 cm^{-1} for S-CN and O-CN, implying the sizable conjugated system of tri-s-triazine units and indeed modification of the pyrolysis process. Furthermore, it is well known that the broad peak located in the range of 3000–3700 cm^{-1} belongs to the stretching modes of uncondensed amino groups and adsorbed H_2O molecules [24]. As seen from FT-IR, the peak area is depressed for S-CN and O-CN under the same conditions, indicating more condensation of CN in the presence of supramolecular precursors and less pending nitrile groups compared to their counterparts CN-ML and CN-TU. Hence, the thermal polymerization of MCT avoids the sublimation of the intermediate during heating and thus gives a satisfactory process toward the formation of carbon nitride.

The typical XRD diffraction peaks of carbon nitride that appear around 27.4 and 13.1° are assigned to interplanar stacking unit (002) systems along with the c-axis, and an in-plane structural packing motif (nitrogen pots), respectively, as shown in Fig. 4j [16]. The less intense (002) peak in the S-CN sample and a negative shift imply that the sheet-like structure is exfoliated while increasing the interlayer distance. Moreover, the (100) peak for the S-CN sample is significantly widened,

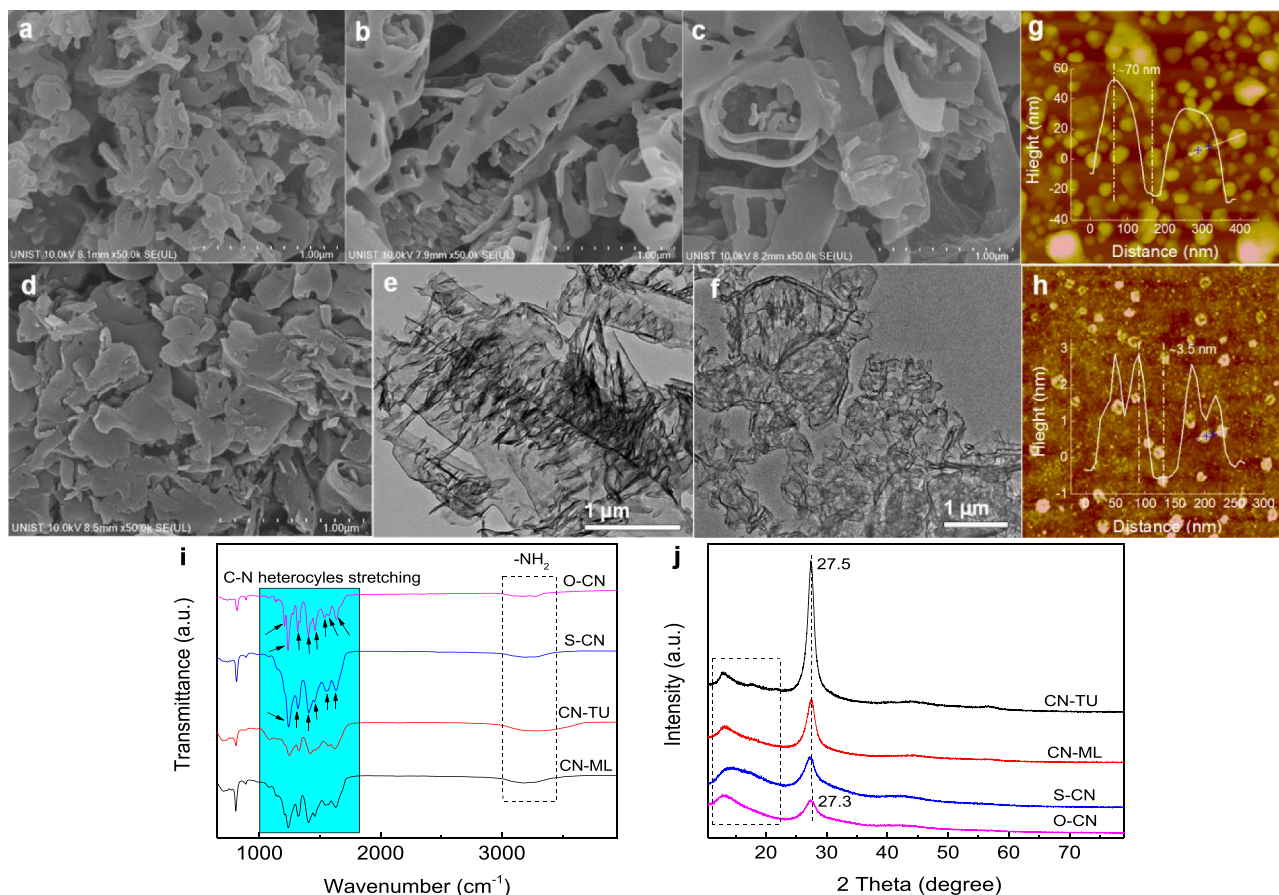


Fig. 4. SEM images of S-CN with different TU contents (a) S-CN (3, 3, 1.32), (b) S-CN (3, 3, 3), and (c) S-CN (3, 3, 4.68); (d) SEM image of S-CN after thermal treatment under air atmosphere (O-CN); TEM images of (e) optimized S-CN (3, 3, 3), and (f) O-CN; AFM images and the corresponding thickness analysis results of (g) CN-ML, and (h) O-CN; (i) FT-IR spectra, and (j) XRD patterns of CN-ML, CN-TU, S-CN, and O-CN.

which may be related to high surface tension due to sulfur doping sites in the nitrogen pots and fluctuations within the atomic structure. The parameters of dislocation density (δ) and strain (ϵ) were estimated based on the plane (100) (Table 1). As is evident, the S-CN exhibits a higher value of dislocation density and strain than CN-ML and CN-TU, which can result from the presence of sulfur with a larger atomic size in the backbone, causing more fluctuations in atomic sheets. These results are in agreement with the TEM and SEM images of S-CN. For O-CN, the interplanar stacking unit shifts from 27.5° to 27.3° (Fig. 4j). At the same time, the intensity decreases, illustrating that the stacking of tri-s-triazine layers has disappeared and the distance between layers has increased. Furthermore, the width of the (100) plane for O-CN is noticeably decreased than that of S-CN. A similar decreasing trend is also observed in O-CN's dislocation density and strain factors (see Table 1). This phenomenon could result from sulfur replacement with oxygen atoms having a smaller atomic size similar to nitrogen in the framework of carbon nitride, endowing less surface tension and fluctuating in every single nanosheet. These alterations in the nanostructure can be inferred from the SEM and TEM results.

The high resolution C1s XPS results for the materials CN-ML, CN-TU, S-CN, and O-CN, are shown in Fig. 5a, in which the binding energy of the adventitious carbon is considered at 284.8 eV. The high resolution C1s spectrum of CN-ML shows two typical peaks at 284.8 and 288.1 eV, associated with C-C and C-N=C groups [25,26]. The ratios of N-C=N to C-C for samples of O-CN, S-CN, CN-TU, and CN-ML are 7.41, 4.27, 1.93, and 2.03, respectively. Taking into account the increased exfoliation of the O-CN sample, as confirmed by TEM and XRD, the enhanced ratio of N-C=N to C-C indicates highly condensed tris-triazine units in the nanosheets. This is very helpful in enhancing the light harvesting ability of O-CN to produce more photogenerated carries. The N1s spectrum is also deconvoluted into three peaks at 398.7, 399.7, and 401.0 eV, which are related to C=N-C, N-(C)₃, and N-H pending groups, respectively (Fig. 5b) [27]. Furthermore, the weak peak centered at 404.5 eV is associated with π excitations [24]. In this case, the ratio of C=N=C to N-(C)₃ for O-CN, S-CN, CN-TU and CN-ML samples is 5.52, 6.50, 1.22 and 1.21, respectively. This means that significant improvement occurs in the building blocks of carbon nitride using the three monomers. The C1s and N1s peaks corresponding to the carbon nitride building blocks in S-CN become more pronounced than their counterparts. Furthermore, the N-(C)₃ position dramatically moves to higher binding energy, showing that the electron density is decreased around N-(C)₃ groups (inset arrow in Fig. 5b). The high resolution S2p spectrum of S-CN shows a sulfur peak at 163.9 eV in CN-TU and S-CN, which are associated with the C-S bond in the carbon nitride material (Fig. 5c) [28,29]. Interestingly, no sulfur is observed in the S2p XPS of O-CN, indicating that thermal treatment at high temperature in an air atmosphere leads to the release of the remaining sulfur from the carbon nitride framework. The magnified FT-IR spectra of O-CN indicate an additional peak located at 1280 cm^{-1} , compared to S-CN, which is assigned to the stretching vibration of C-O-C and oxygen doping (Fig. 5d) [30,31]. Therefore, the shift of N-(C)₃ to higher binding energies in O-CN can originate from two main phenomena: (i) more condensation of heptazine rings confirmed by XPS and elemental analysis, noting that more nitrogen atoms with sp^2 hybridization around the

N-(C)₃ site (sp^3 hybridization) might withdraw more electrons from the N-(C)₃, and consequently positive movement occurs; and (ii) doping of oxygen atoms into the heptazine ring through weaker C-S bonds at high temperature under air atmosphere (insert in Fig. 5d). As a result, more heptazine units and oxygen atoms might provide a more visible light-harvesting antenna for carbon nitride. The results of XPS element analysis are (total C = 48.41, N = 49.43, O = 2.07, and S = 0.18%) for CN-TU, (C = 46.91, N = 51.26, and O = 1.83%) for CN-ML, (C = 49.06, N = 48.89, O = 1.82%, S = 0.23%) for S-CN, and (C = 50.57, N = 47.17, and O = 2.26%) for O-CN.

3.2.2. DFT calculations

To deeply understand the effect of the sulfur or oxygen doping site on the structural, energetic, and electronic features of carbon nitride, DFT calculations for CN-ML, S-CN, and O-CN were performed. In Table 2, it is found that O-CN has the highest stability with a more negative binding energy ($\Delta E_{\text{binding}}$) than S-CN. These data are completely consistent with characterization results such as XPS and FT-IR, where the C-S doping site disappeared while the C-O functional group emerged. Therefore, oxygen doping in the framework presents carbon nitride with a more stable structure than sulfur doping, suggesting replacing the C-S functional group with C-O in a static air atmosphere. The optimized structures, the HOMO and LUMO orbitals of the CN-ML, S-CN, and O-CN structures, are shown in Fig. 6. The HOMO and LUMO orbitals of CN-ML are symmetric, whereas the distribution of electric charge is more asymmetric for the structures of S-CN and O-CN. Therefore, it might accelerate the separation of the charge carrier after sulfur or oxygen doping [32]. For a quantitative comparison of the sulfur doping effect and oxygen doping, the dipole moments (μ , Debye) for the structures of CN-ML, S-CN, and O-CN were also calculated and reported in Table 2. The μ values obviously show that the O-CN compound has the highest dipole moment, unveiling that the electric charge distribution is much more asymmetric than S-CN. This shows that doping of the O atoms within the CN backbone might enhance electron density and charge mobility more than S atoms.

3.2.3. Texture properties of CNs

All samples indicate mesopore behavior with a well-resolved H3-type hysteresis loop associated with aggregates of plate-like particles giving rise to a slit-shaped pore (Fig. 7a). This type of pores is a rigidly connected collection of loosely coherent particles with no limitation of adsorption at high P/P_0 ($0.9 < P/P_0 < 1$), suggesting the presence of large mesopores and macropores. This behavior was well-matched with the pore size distribution curve, as depicted in Fig. 7a. Compared to CN-TU ($9.5\text{ m}^2\text{ g}^{-1}$) and CN-ML ($5.8\text{ m}^2\text{ g}^{-1}$), S-CN clearly shows more nitrogen intake with a BET surface area of $30.6\text{ m}^2\text{ g}^{-1}$ (Table 3). Therefore, the use of supramolecular self-assembly also modifies the textural properties of carbon nitride to some extent. The sample of O-CN prepared under static air atmosphere show dramatic improvement in the surface area ($153.6\text{ m}^2\text{ g}^{-1}$) and the pore volume ($0.71\text{ cm}^3\text{ g}^{-1}$). A new and homogeneous set of pores size centered at 39 nm is observed for O-CN, which probably originates from the aggregation of nanosheets with less fluctuation as confirmed by SEM and XRD results. Such a great nanoarchitecture provides plenty of available pores for target molecules and also improves light capture through multiple scattering effects [33].

3.2.4. Optical properties of CNs

The optical properties of S-CN and O-CN were compared with those of other samples by UV-vis spectra results (Fig. 7b). Based on the Kubelk-Munk function (Fig. S7), the band gap energies (E_g) of all samples are summarized in Table 3. It should be noted that CN-TU (2.61 eV) shows an Urbach tail compared to CN-ML (2.69 eV), attributing to the midgap states located within the band gap [29,34]. Despite the decreased band gaps of CN-ML and CN-TU, both samples suffer from poor textural properties and fast recombination of electron-hole pairs. In contrast, S-CN reveals a blue shift in the absorption edge and an

Table 1

The dislocation density (δ) and strain (ϵ) parameters were estimated based on the (100) XRD plane, and the texture of the surface composition originated from XPS.

Sample	2 θ	FWHM	$\delta \times 10^{-3}$ (nm^{-2})	$\epsilon \times 10^{-3}$	N-C=N/ C-C	C-N=C/ N-(C) ₃
CN-TU	13.1	2.1	5.6	79.8	1.93	1.22
CN-ML	13.1	3	11.4	114.0	2.03	1.21
S-CN	13.1	5.7	41.2	216.6	4.27	6.50
O-CN	13.1	3.4	14.6	129.2	7.41	5.52

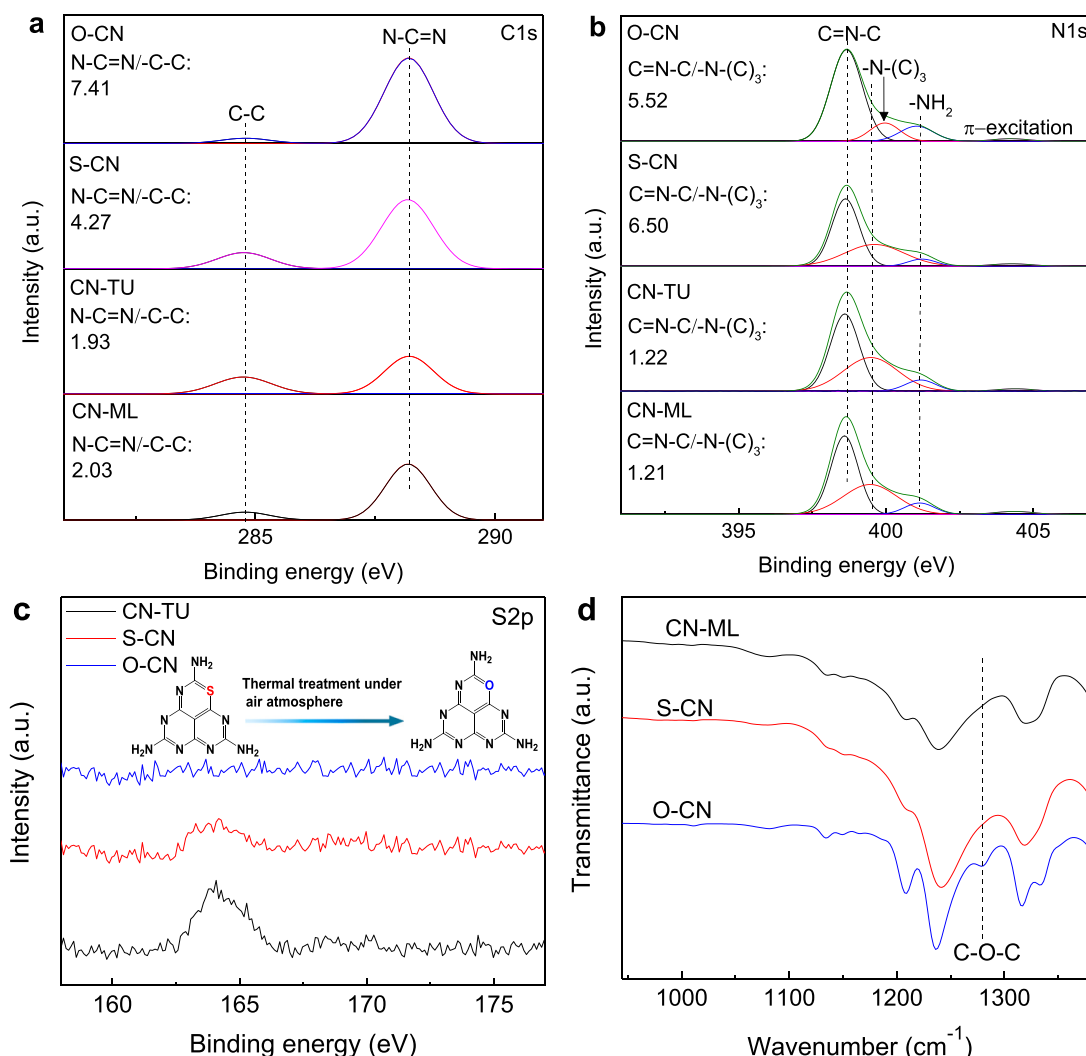


Fig. 5. (a) & (b) High resolution XPS spectrum of C1s and N1s for CN-ML, CN-TU, S-CN, and O-CN; (c) High resolution XPS spectra of S2p for CN-TU, S-CN, and O-CN; (d) The magnified FT-IR of CN-ML, S-CN, and O-CN.

Table 2

Binding energies ($\Delta E_{\text{binding}}$, kcal mol⁻¹), dipole moments (μ , Debye), E (HOMO), E (LUMO) and band gaps for CN-ML, S-CN and O-CN compounds.

Compound	$\Delta E_{\text{binding}}$	μ (Debye)	E (HOMO)	E (LUMO)	E_g (eV)
CN-ML	-8859.321	1.6613	-6.488	-2.609	3.839
S-CN	-8734.266	5.1315	-4.300	-2.595	1.705
O-CN	-8808.226	5.2510	-4.112	-2.512	1.600

increased band gap of 2.73 eV. Although previous studies and our DFT calculations reveal that nonmetal doping in the carbon nitride backbone decreases the band gap [35] nevertheless, S-CN synthesized in this study shows an increased value. This result is attributed to the strong quantum confinement effect because the prepared S-CN from the supramolecular complex gives carbon nitrides a much smaller particle size. Furthermore, S-CN reveals an enhanced absorption tail from 450 to 790 nm, compared to CN-TU and CN-ML. Interestingly, the band gap energy for O-CN (2.83 eV), which has a larger surface area and pore volume, is higher than that in S-CN (2.73 eV). Meanwhile, the color of the O-CN sample changes from light gray to white-yellow, which is consistent with the absorbance change (Fig. 7b). This blue shift is completely confirmed by SEM and TEM results, where the particle size and stacking layers were significantly decreased, and ultrathin nanosheets appeared. Extended absorption in the case of O-CN can be the result of three main reasons.

First, there is the presence of midgap states originating from oxygen doping sites. Second, the efficient polycondensation process and consequently more heptazine building block units, as confirmed by XPS and FT-IR. Third, exceptional textural properties such as the highest surface area and pore volume with ultrathin nanosheets can provide more opportunities to harvest light irradiation. Therefore, despite the wider band gap of S-CN, a combination of supramolecular strategy and nonmetal doping successfully leads to a strong band edge tail up to 790 nm and enhancement of the light harvesting capability.

3.2.5. Separation and transport of charge carrier

The effect of a dual combination of O-doped heptazine units and principle modification of the polycondensation process can be further investigated on the separation and transfer of electron-hole pairs via steady-state photoluminescence (PL) spectroscopy, as well as electrochemical techniques. The steady-state PL emission provides more information about the deactivation pathways of charge carriers since the decrease in emission intensity is related to the depressing of the recombination of electron-hole pairs [36,37]. Compared to CN-ML, CN-TU shows a lower peak intensity of PL, confirming that the midgap states induced by sulfur doping accelerate the separation of electron-hole pairs (Fig. 7c). On the other hand, a lower PL peak intensity for S-CN is observed compared to that of CN-TU, suggesting a suppressed charge carrier recombination and an increasing charge

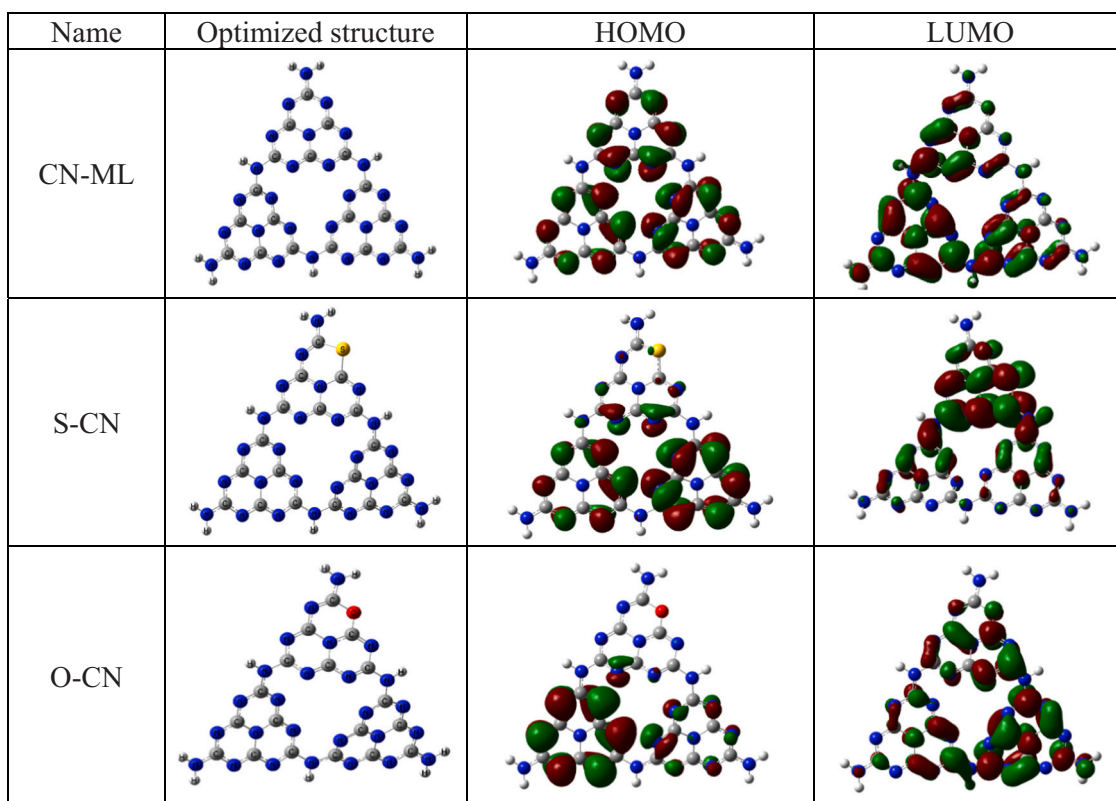


Fig. 6. Optimized structures, HOMO and LUMO orbitals distribution for compounds CN-ML, S-CN and O-CN computed at the level B3LYP/6-31 +G (d).

diffusion rate in the heptazine aromatic system. Furthermore, the smallest PL peak intensity was found for O-CN among all samples, indicating its lowest recombination rate. Indeed, O-CN with sizable conjugated heptazine units and its ultrathin thickness and excellent texture architecture shortens the charge diffusion length and accelerates the transfer of charge carriers. Moreover, the extra electrons of the incorporated oxygen atom are delocalized in the conjugated aromatic system, increasing the charge density and mobility [38]. Thus, the O-CN is taking full advantage of the fundamental improvement of the polycondensation process, the presence of oxygen doping sites with midgap states, and the high exfoliation of nanosheets.

From Fig. 7d, the S-CN sample with new morphology clearly shows smaller electrochemical impedance spectroscopy (EIS) semicircle radius than the CN-ML and CN-TU materials, revealing less charge resistance and more effective charge transfer at the double layer. Hence, the self-assembly structure opens new channels for improving the charge transitions compared with common structures. An even more decreasing EIS semicircle is observed in the case of the O-CN sample, indicating that oxygen doping decreases the level of electron-hole recombination and enhances the charge mobility within the tri-s-triazine surface. Furthermore, an O atom has one more electron than an N atom, producing extra electrons throughout the CN structure, improving charge carrier transitions [17]. This enhancement is also in agreement with the results of the textural and structural properties, since more surface area of S-CN and O-CN might be the reason for improving the EIS performance by providing sufficient active sites and accelerating mass transfer phenomena. On the other hand, when the optimized TU content, that is, 3 g, is changed to 1.32 or 4.68 g, the EIS semicircles are more pronounced, implying that TU molecules play a vital role in controlling the electron-hole recombination (Fig. S8a). Interestingly, the BET isotherms of S-CN (3, 3, 1.32) and S-CN (3, 3, 4.68) indicate similar textural features, such as surface area and pore volume, compared to the optimized sample S-CN (3, 3, 3) (Table S1). This is a clue to the importance of TU molecules presented in the self-assembly to improve charge transfer. For

more clarification, the transient photocurrent responses with on-off mode were also recorded for the mentioned materials at 0.6 V vs Ag/AgCl. S-CN shows the highest current trend compared to the CN-ML and CN-TU samples and the performance is increased after thermal treatment (O-CN). It indicates that a change in ultrathin nanosheet morphology and oxygen doping in the case of O-CN strongly improves photocurrent performance (Fig. 7e). Furthermore, the sample with optimized TU content has the highest photocurrent intensity than the other TU contents with the same textural properties (Fig. S8b). These results confirm that the collaboration of TU, ML, and CY in self-assembly drastically improves photocatalytic properties.

However, because the above results highlight the high separation efficiency of photogenerated electron-hole pairs in O-CN, further investigation was done to obtain a deep insight into the charge transfer efficiency. Here, the Mott-Schottky analysis was carried out to estimate the donor concentrations in the as-prepared samples and provide more information about charge transport behavior. The Mott-Schottky plots of the CN-ML, CN-TU, S-CN, and O-CN films with a frequency of 1 kHz are presented in Fig. 7f. All electrodes exhibit positive slopes with n-type characteristics, reflecting that electrons are the major carriers to the surface. The donor concentration (or electron density) can be determined by applying the Mott-Schottky equation (Eq. (1)).

$$\frac{1}{C^2} = \frac{2}{\epsilon \epsilon_0 A^2 e N_D} \left(V - V_{fb} - \frac{k_B T}{e} \right) \quad (1)$$

Where C is the capacitance of the space charge (F cm^{-2}), e is the electron charge ($1.60 \times 10^{-19} \text{ C}$), ϵ_0 is the vacuum permittivity ($8.854 \times 10^{-14} \text{ F cm}^{-2}$), ϵ is the relative permittivity (4.6 for g-C₃N₄), k is the Boltzmann constant ($1.38 \times 10^{-23} \text{ J K}^{-1}$), N_D is the donor concentration per unit volume (cm^{-3}), T is the absolute temperature, V is the applied electrode potential. V_{fb} is the flat-band potential at the semiconductor/electrolyte interface. The electron density of CN-ML, CN-TU, S-CN, and O-CN films were calculated to be 3.3×10^{22} , 3.5×10^{22} , 3.8×10^{22} , and 4.5×10^{22} . O-CN shows a much higher electron density, which indicates

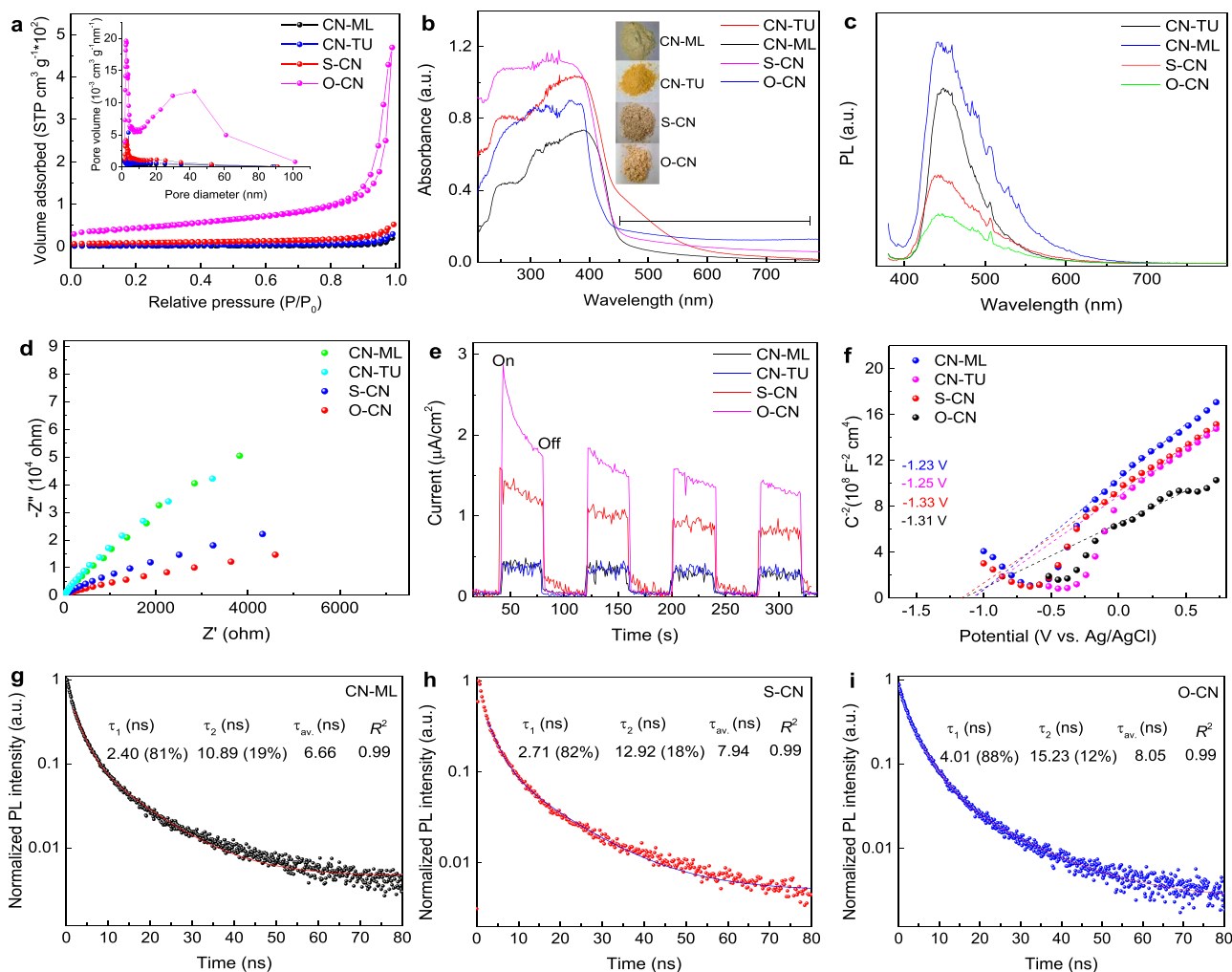


Fig. 7. (a) N₂ adsorption–desorption isotherms, (b) UV–vis light absorption spectra, (c) PL spectra, (d) EIS Nyquist plots, (e) Photoelectrochemical responses, and (f) Mott-Schottky plots of CN-ML, CN-TU, S-CN, and O-CN; (g-i) Time-resolved PL spectra of (CN-ML, S-CN, and O-CN along with fitting data.

Table 3

Textural and optical properties of synthesised materials' surface composition and the extracted results from the Mott-Schottky plots.

Sample	S.A. ^a (m ² g ⁻¹)	P.D. ^b (nm)	P.V. ^c (cm ³ g ⁻¹)	E _g (eV)	N _D (cm ⁻³)	V _{fb} (V vs. Ag/ AgCl)	W _{sc} (nm)
CN-TU	9.7	17.4	0.045	2.61	3.5 × 10 ²²	-1.23	15.5
CN-ML	5.8	28.1	0.030	2.69	3.3 × 10 ²²	-1.25	15.9
S-CN	30.6	13.5	0.076	2.73	3.8 × 10 ²²	-1.33	15.2
O-CN	153.6	20.1	0.71	2.83	4.5 × 10 ²²	-1.31	13.9

^a Surface area (BET), ^b Average pore diameter (BJH), and ^c Pore volume.

that dual oxygen doping and the modified polycondensation process lead to a significant increase in the carrier density. The highest N_D value for O-CN may be due to the redistribution of extra electrons from oxygen atoms and its delocalization among the π -conjugated electronic structure. Ran et al. reported a similar result, suggesting that lone electron pairs of incorporated P delocalized to the P-doped aromatic system increased charge density and mobility [39]. Moreover, O-CN also indicated highly condensed heptazine aromatic units, strengthening the π -delocalized electronic system and consequently improving the number of charge carriers.

The E_{fb} (vs Ag/AgCl) values were estimated by extrapolating the X-intercepts of the liner region in Mott–Schottky plots. The E_{fb} values of CN-ML, CN-TU, S-CN, and O-CN are calculated to be -1.23, -1.25, -1.33,

and -1.31 V, which are equivalent to -1.03, -1.05, -1.13, and -1.11 V (vs NHE), respectively [40]. The value of E_{fb} is usually close to CB and is located below the CB level of n-type semiconductors. The negative shift of E_{fb} is more favorable for reduction half-reactions, better charge separation, and its accumulation in the electrode.

The situation in which a semiconductor is immersed in the electrolyte leads to a space charge region in the semiconductor-electrolyte junction. The width of the space charge region (W_{sc}) is obtained by solving Poisson's equation, depending on the electron density and the flat-band potential (Eq. 2) [41].

$$W_{sc} = \sqrt{\frac{2\epsilon\epsilon_0(V - V_{fb})}{eN_D}} \quad (2)$$

Table 3 comparatively summarizes the V_{fb} and N_D, and W_{sc} values of the prepared samples. The W_{sc} values of CN-ML, CN-TU, S-CN, and O-CN are 15.9, 15.5, 15.3, and 13.9 V, respectively. The narrowest of the W_{sc} for O-CN since ultrathin nanostructures decrease charge-to-surface diffusion length, and the outstanding optical and physical properties give rise to an acceleration of interfacial charge transfer from the electrode to the electrolyte.

To further elucidate the participation of charge carriers and their lifetimes in photocatalytic performance, time-resolved transient photoluminescence (TRPL) decay spectra of O-CN, S-CN, and CN-ML were recorded as shown in Fig. 7g–i. The TRPL decay curves are fitted by the following biexponential model (Eq. (3)), where τ_1 and τ_2 are the short

and long lifetime, respectively, while A_1 and A_2 are the corresponding amplitudes. By having τ_1 and τ_2 , the samples' average lifetime ($\tau_{av.}$) is calculated using the Eq. (4) [7].

$$I(t) = A_1 \exp(-t/\tau_1) + A_2 \exp(-t/\tau_2) \quad (3)$$

$$\tau_{av.} = (A_1 \tau_1^2 + A_2 \tau_2^2) / (A_1 \tau_1 + A_2 \tau_2) \quad (4)$$

In detail, all the TRPL decay results fitted along with their percentages were listed in the insert of Fig. 7g–i. It is believed that short and long lifetimes are associated with nonradiative recombination of charge carriers and interband recombination of photogenerated excitons, respectively. It should be noted that nonradiative relaxation is governed by several structural features such as foreign atoms, local defects, and the insertion of metal into the cavity [39]. All of these phenomena can open a new deactivation channel competing with the PL emission.

Among all samples, O-CN shows an increased τ_1 (4.01 ns) and τ_2 (15.23 ns) compared to S-CN ($\tau_1 = 2.71$ ns, $\tau_2 = 12.92$ ns) and CN-ML ($\tau_1 = 2.40$ ns, $\tau_2 = 10.89$ ns) (Fig. 7g–i), implying that O-CN elongates the average lifetime of charge carries and accelerates charge separation. What is more interesting, the nonradiative percentage of O-CN is 88%, which is much higher than that of S-CN (82%) and CN-ML (81%). This implies that the foreign oxygen atom in O-CN increases midgap states. In addition, its local positions within the band structure facilitate the number of nonradiative relaxations, which is very helpful for

photocatalytic efficiency. These observations are consistent with the electrochemical results.

3.2.6. Evaluation of photocatalytic activity

Table S1 shows the photodegradation results of S-CN samples with different TU contents in the photodegradation of RhB. In view of the textural properties, the specific surface area of S-CN is around (3 and 5)-fold more than that of CN-TU and CN-ML, respectively. One might expect that the photocatalytic enhancement comes from the larger surface area and consequently increased photocatalytic active sites and mass transfer. The textural property is one of the most important factors in improving photocatalytic activity. However, the textural characteristics of the two other supramolecular assemblies with different TU content showed similar surface area, porosity and lower photo activities (Table S1). Hence, it seems that the different photocatalytic behaviors of the resulting S-CN samples may result from the presence of TU molecules and sulfur doping and their role in organizing the parent supramolecular assembly. As shown in Fig. 8a, no significant degradation of RhB is observed without light irradiation, while CN-ML and CN-TU only degrade 55% and 60% in 50 min, respectively, under visible light irradiation. Compared to CN-ML and CN-TU, S-CN exhibits enhanced visible light photodegradation of RhB up to 95% after irradiation for 25 min. This visible light performance can be attributed to highly condensed heptazine units and consequently more available light harvesting.

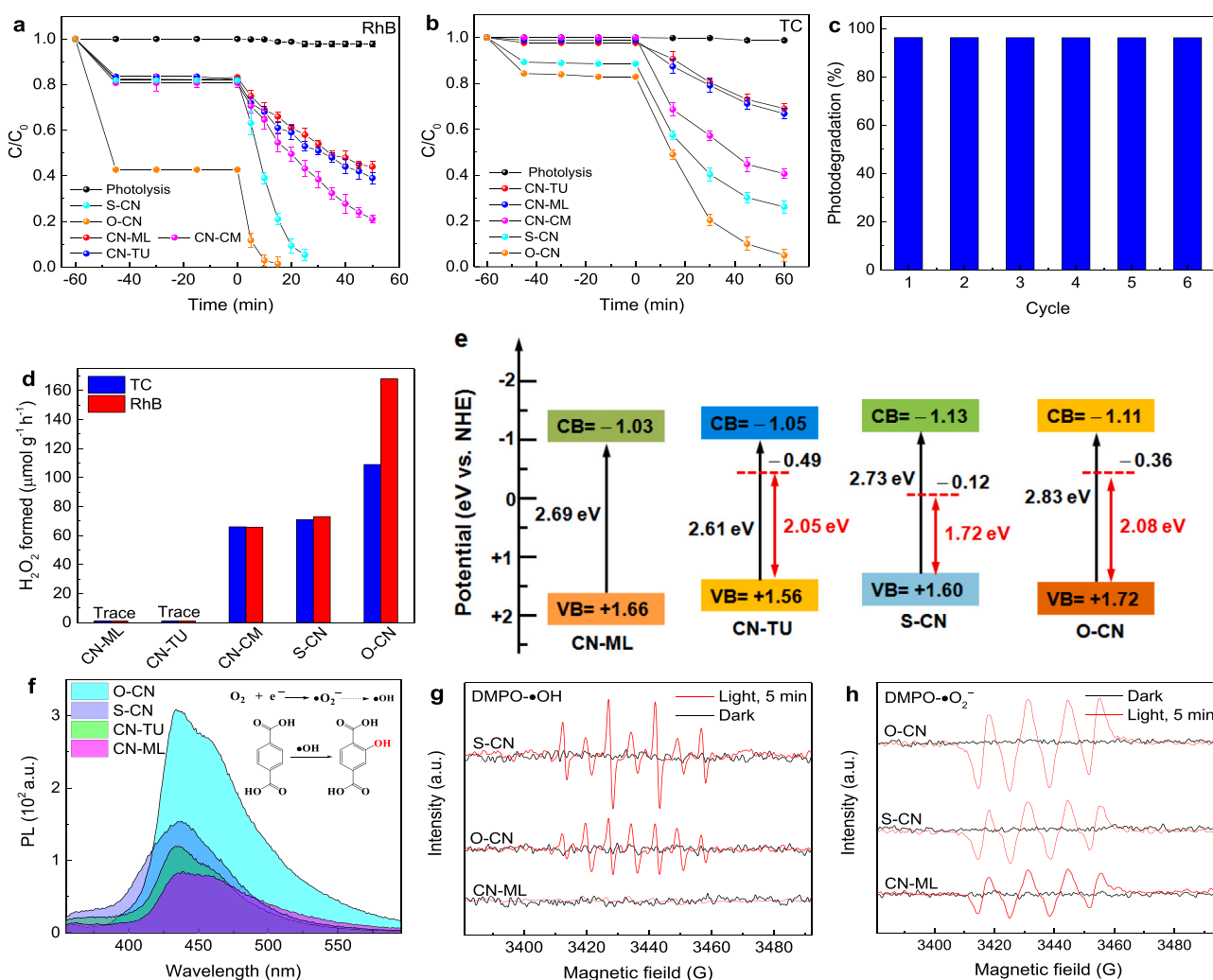


Fig. 8. Photocatalytic degradation of (a) RhB, and (b) TC for CN-ML, CN-TU, CN-CM, S-CN and O-CN; (c) Recyclability of the O-CN in six experiments for the photocatalytic degradation of RhB under visible light irradiation; (d) Photocatalytic production of H_2O_2 ; (e) energy band structures, (f) the PL spectra of the produced 2-hydroxyterephthalic acid over CN-ML, CN-TU, CN-CM, S-CN; (g–h) ESR spectra of CN-ML, S-CN, and O-CN under dark and visible light illumination.

Furthermore, the effect of thiourea on the supramolecular complex would be clearer when comparing the photodegradation of RhB over CN-CM (57%) and S-CN (95%) in 25 min, unmasking that TU plays a key role in improving performance. From Fig. 8a, O-CN indicates unprecedented photoactivity toward RhB (100%) in a short time of 15 min under visible light irradiation, compared to the other samples. It should be noted that the reaction rate constant of O-CN is about 19.3 and 2.2 times greater than that of CN-ML and S-CN in the degradation of RhB under visible light irradiation, respectively (Fig. S9a). Furthermore, O-CN exhibits the highest activity in the degradation of TC (more than 95%), compared to CN-ML (31%), CN-TU (34%), CN-CM (60%) and S-CN (74%) (Fig. 8b). The reaction rate constant of O-CN, in the case of TC, is also 8.0 and 2.4 times higher than that of CN-ML and S-CN (Fig. S9b).

TOC analysis was also performed to investigate the ability of metal-free O-CN for the mineralization of TC (Fig. S9c). TOC removal over O-CN reached approximately 46.2% in 60 min under visible light irradiation, while only around 8.9% can be seen for CN-ML. Hence, O-CN with fundamental engineering can mineralize TC more effectively.

Because the recyclability of heterogeneous photocatalysts makes them unique compared to homogeneous photocatalysts, the stability of the O-CN was assessed. As shown in Fig. 8c, the degradation results are repeatable several times without any apparent depreciation after six successive recycles for the degradation of RhB under visible light irradiation. This implies that the O-CN has high stability during the recycling process, such as washing with deionized water, centrifuging, and drying. It can be evidenced by comparing the XRD and FT-IR results of fresh O-CN and after the sixth cycle (Fig. S9d–e), which indicate no significant change in the chemical structure. Tables S2 and S3 summarize the comparison of the experimental conditions and performance of recently reported photocatalysts for the photodegradation of RhB and TC with O-CN prepared in this study.

Furthermore, H_2O_2 only produces water and oxygen as side products. Therefore, in situ photocatalytic production of H_2O_2 can ensure long-term disinfection capacity in water during the photodegradation process [42]. Here, the photocatalytic production of H_2O_2 was further investigated during photodegradation of RhB and TC without a sacrificial agent in an open air atmosphere. Fig. 8d presents the amounts of H_2O_2 generated in 1 h on the prepared samples under visible light irradiation. While CN-ML and CN-TU produced a negligible amount of H_2O_2 , S-CN indicates a much higher activity for H_2O_2 production (around $73 \mu\text{mol g}^{-1} \text{h}^{-1}$) during RhB and TC degradation. Interestingly, the H_2O_2 production rate is further increased to the highest level in the presence of RhB ($168 \mu\text{mol g}^{-1} \text{h}^{-1}$) and TC ($109 \mu\text{mol g}^{-1} \text{h}^{-1}$) over the O-CN photocatalyst. This observation indicates that RhB molecules with carboxyl groups (COOH), compared to TC, efficiently suppress the decomposition of H_2O_2 and accelerate its desorption from the O-CN surface. Similarly, abundant carboxyl and hydroxyl groups have been reported to be helpful for the desorption of H_2O_2 formed [42]. However, very few reports have been on visible light photocatalytic oxidation of H_2O to H_2O_2 without sacrificial agents and blowing of O_2 . To get initial information about H_2O_2 production without sacrificial agents, recently reported photocatalysts for H_2O_2 production are shown in Table S4. These findings further confirm that the combination of oxygen doping sites, the modified polycondensation process, and impressive texture nanoarchitecture enhances the universality of photocatalytic performance to a great level for both degradation and H_2O_2 production under visible light irradiation.

3.2.7. Study of the active species and reduction ability of electrons on O-CN

To reveal the ability of the photocatalyst to promote photocatalytic performance, we estimated the band structure of samples along with their possible midgap states based on the Tauc plots and Mott-Schottky curves. According to the Tauc plot, the calculated band gap energy values for CN-ML, CN-TU, S-CN, and O-CN are 2.69, 2.61, 2.73, and 2.83 eV, respectively. Moreover, the position of the transition energy (E_t) from VB to the midgap can be further extracted from Tauc plots as

displayed in Fig. S7 [39]. E_t values for CN-TU, S-CN, and O-CN are calculated to be 2.05, 1.72, and 2.08 eV, respectively. Consequently, the CB potentials of O-CN and CN-ML, CN-TU, S-CN, and O-CN are estimated to be -1.03 , -1.05 , -1.13 and -1.11 V using the Mott-Schottky curves. Therefore, the VB edge potential of CN-ML, CN-TU, S-CN, and O-CN is 1.66, 1.56, 1.60, 1.72 V via the formula of $E_{VB} = E_{CB} + E_g$, respectively. In addition, the midgap positions are -0.49 , -0.12 and -0.36 for CN-TU, S-CN, and O-CN, respectively. Interestingly, the midgap position O-CN is shifted to a more negative value compared to S-CN. A schematic of the band structure of the samples is shown in Fig. 8e. As is evident from electrochemical measurements, the O-CN showed the highest electron density and more negative flat-band potential and midgap states than bulk samples. It indicates that electrons in the CB and midgap states of O-CN theoretically provide enough driving force for a specific half-reaction of superoxide radical production ($\text{O}_2/\bullet\text{O}_2^-$) = -0.33 V vs NHE) [43].

To obtain fundamental insight into the midgap states, the total density of states (TDOS) spectra of CN-ML, S-CN, and O-CN compounds are illustrated in Fig. S10. CN-ML indicates the highest value of band gap compared to S-CN and O-CN compounds. Furthermore, some new midgap energy levels appear between the HOMO and LUMO orbitals of S-CN and O-CN compounds, confirming that both sulfur and oxygen doping create midgap energy levels, and consequently, E_g values are decreased. Interestingly, a comparison of the PDOS spectra of S-CN and O-CN shows that oxygen doping leads to a new energy level close to CB (LUMO), compared with sulfur doping. As a result, oxygen doping presents the midgap energy with more thermodynamically favorable energy for reduction reactions. In other words, the photoexcited electrons on the O-CN might easily move from the impurity states to the target half-reactions.

The results of the scavenging experiment for the photodegradation of RhB and TC are shown in Fig. S11. These indicate that when IPA is added as a $\bullet\text{OH}$ scavenger, no change is observed in the degradation performance of RhB and TC, demonstrating that $\bullet\text{OH}$ is not an active species primarily. Although the addition of TEOA as the hole scavenger somewhat influences the photocatalyst efficiencies, it nonetheless does not play a pivotal role in degradation. After adding BQ, as a well known $\bullet\text{O}_2^-$ scavenger, the photodegradation process for both contaminants almost stopped. This result strongly confirms that $\bullet\text{O}_2^-$ plays a key role in photodegradation [44]. For further clarification, the reduction capacity of electrons was evaluated by monitoring the $\bullet\text{OH}$ radicals generated in the presence of TEOA to capture holes in the liquid solution. Generally, $\bullet\text{OH}$ can be generated indirectly via electrons of CB, i.e., $\text{O}_2/\bullet\text{O}_2^-/\bullet\text{OH}$ (-0.33 V vs NHE), or directly by holes of VB, $\text{OH}^-/\bullet\text{OH}$ (1.99 V vs NHE) [45]. The PL technique was applied to detect $\bullet\text{OH}$ through Terephthalic acid (TA) as a probe molecule. TA without a PL signal readily converts to 2-hydroxyterephthalic acid with a pronounced signal around 450 nm, after reacting with $\bullet\text{OH}$ in the water. Remarkably, the O-CN indicates a stronger peak than that of CN-TU and CN-ML, manifesting the strong reduction feature of photogenerated electrons and more electron density on the surface of O-CN (Fig. 8f). These results suggest that the photocatalytic behavior is significantly dependent on the property of the electron on the CB that attacks the oxygen in the water to produce $\bullet\text{O}_2^-$ species.

The EPR spectrum was recorded to further investigate the active species generated on the O-CN, S-CN, and CN-ML. As shown in Fig. 8g and h, there is no obvious signal related to $\text{DMPO}\cdot\bullet\text{OH}$ and $\text{DMPO}\cdot\bullet\text{O}_2^-$ in EPR under dark conditions. However, after visible light irradiation, as shown in Fig. 8g, while CN-ML does not show any obvious signal, both S-CN and O-CN unveil the characteristic signals associated with $\bullet\text{OH}$ radicals in $\text{DMPO}\cdot\bullet\text{OH}$. As discussed in the PL probing results, $\bullet\text{OH}$ radicals can be generated indirectly by reacting the CB's electrons with oxygen to produce $\bullet\text{O}_2^-$ and subsequently $\bullet\text{OH}$ radicals. More importantly, O-CN exhibits the highest EPR intensity of $\text{DMPO}\cdot\bullet\text{O}_2^-$ compared to other samples, suggesting much greater electron reduction ability on the CB of O-CN as confirmed with electrochemical measurements and PL

probing technique.

3.2.8. Possible photocatalytic mechanism

Since TC is hardly mineralized, identifying the intermediates and their toxicity during photocatalytic degradation is in high demand and provides insight into its degradation mechanism. Hence, the intermediate identification, mechanism degradation of TC, and also the toxicity of the intermediates were deeply discussed in the Figs. S12–14.

With all the results above in hand, a potential photocatalytic mechanism is proposed over the O-CN photocatalyst, as shown in Fig. 9. As a matter of fact, a boosted photocatalyst should fulfill some critical requirements: (i) to harvest photons from a wide range of the solar spectrum and generate much more photogenerated electron-hole pairs, (ii) efficient separation and migration of electron-hole pairs throughout the backbone and surface of the photocatalyst by suppressing surface and volume recombination, (iii) to partake the charge carriers in redox reactions, and (iv) to have a band structure and enough driving force compared with target reactions. Under visible light irradiation, the O-CN can harvest a large portion of the visible light spectrum due to its absorption tail from 450 to 790 nm as well as sizable heptazine units, acting as a light antenna. Moreover, oxygen doping sites, in turn, boost the visible light capacity since oxygen dopants can create midgap states within the band gap and participate by absorption of photons with lower frequencies. Therefore, many electron-hole pairs can be generated over O-CN in comparison to other counterparts. Furthermore, the ultrathin thickness of O-CN nanosheets dramatically shortens the charge diffusion length and accelerates the migration of charge carriers to the surface of the photocatalyst. Afterward, the high concentration of dissolved oxygen molecules in the solution can reach the catalyst surface because O-CN shows the highest surface area and pore volume. Hence, the accumulated electrons on the CB of O-CN react with oxygen to produce the dominant $\bullet\text{O}_2^-$ species (Eq. (3)). Consequently, $\bullet\text{O}_2^-$ radicals attack the TC or RhB and fragment them into very small nontoxic molecules. The $\bullet\text{OH}$ radicals can also be produced indirectly via CB's electrons and contribute to the photodegradation process. The holes in the VB of O-CN can directly degrade organic compounds. Furthermore, photocatalytic production of H_2O_2 can occur through a two-step single-electron O_2 reduction process (Eqs. 5–9) because $\bullet\text{O}_2^-$ species govern the photocatalytic process.

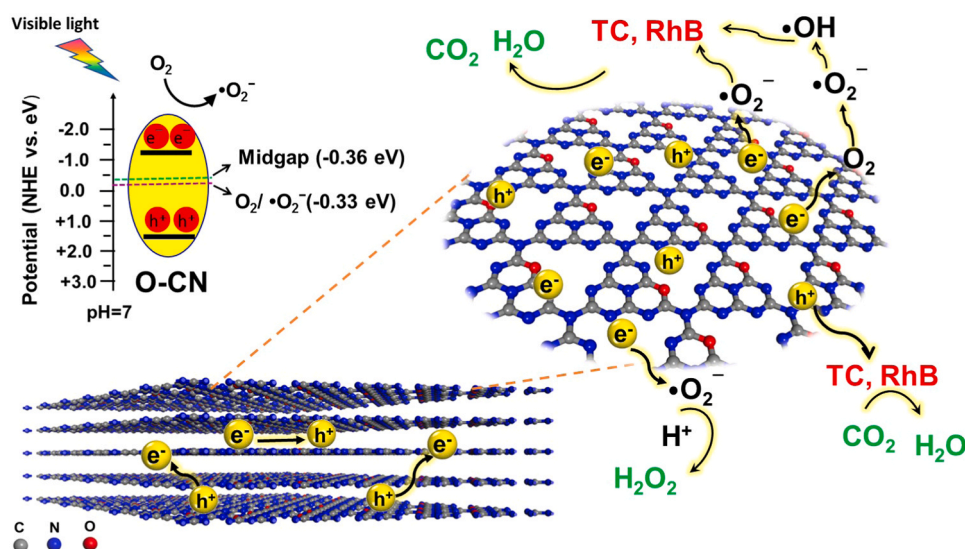


Fig. 9. Schematic illustration of photodegradation of RhB and TC and H_2O_2 production over O-CN under visible light illumination.



4. Conclusions

In summary, a novel supramolecular assembly based on melamine, cyanuric acid, and thiourea under N_2 -assisted polycondensation becomes S-doped carbon nitride (S-CN). Further thermal treatment under a static air atmosphere replaces the S dopant with the O atom. The oxygen doping site gives carbon nitride the highest stability, as confirmed by DFT calculations. The resulting O-CN photocatalyst exhibits excellent visible light harvesting, charge carrier transition, and electronic properties. In addition, it shows the highest electron density at the CB edge, which makes it a strong reduction photocatalyst. This result was further evidenced with more $\bullet\text{OH}$ generation than the control experiments, which was confirmed by PL investigations. Furthermore, O-CN indicated excellent photocatalytic activity in the degradation of RhB (12 mgL^{-1}) and TC (12 mgL^{-1}) under visible light irradiation after 15 and 60 min, respectively. This performance is one of the best-reported efficiencies of the metal-free carbon nitride. Meanwhile, the O-CN generated a highly stable production of H_2O_2 ($168.1 \mu\text{mol g}^{-1} \text{ h}^{-1}$) under an open atmosphere without a sacrificial agent. Furthermore, LC-MS analysis of intermediates during tetracycline degradation confirmed complete degradation of tetracycline to small, nontoxic fragments with a higher lethal dose value (LD_{50}). This work also presents a simple and universal way to introduce oxygen into the backbone of carbon nitride by substituting the sulfur atom.

CRediT authorship contribution statement

Milad Jourshabani: Conceptualization, Methodology, Data curation, Writing – original draft. **Mahdieh Razi Asrami:** Software, Writing – review & editing. **Byeong-Kyu Lee:** Supervision, Writing – review & editing.

Declaration of Competing Interest

The authors declare that they have no known competing financial interests or personal relationships that could have appeared to influence the work reported in this paper.

Acknowledgments

This work was supported by the Brain Pool (BP) fellowship grant funded by the Korea Government (No. 2019H1D3A1A01070060). This work was also supported by the National Research Foundation of Korea (NRF) grant funded by the Korea government (No. 2019R1A2C2085250).

Appendix A. Supporting information

Supplementary data associated with this article can be found in the online version at doi:10.1016/j.apcatb.2021.120839.

References

- [1] M.S. Azami, A.A. Jalil, N.S. Hassan, I. Hussain, A.A. Fauzi, M. Aziz, Green carbonaceous material–fibrous silica–titania composite photocatalysts for enhanced degradation of toxic 2-chlorophenol, *J. Hazard. Mater.* 414 (2021), 125524.
- [2] Y. Zhou, M. Yu, H. Liang, J. Chen, L. Xu, J. Niu, Novel dual-effective Z-scheme heterojunction with g-C₃N₄, Ti₃C₂ MXene and black phosphorus for improving visible light-induced degradation of ciprofloxacin, *Appl. Catal. B* 291 (2021), 120105.
- [3] P. Somathilake, J.A. Dominic, G. Achari, C.H. Langford, J.-H. Tay, Degradation of carbamazepine by photo-assisted ozonation: influence of wavelength and intensity of radiation, *Ozone. Sci. Eng.* 40 (2018) 113–121.
- [4] Y. Wu, X. Zhao, S. Huang, Y. Li, X. Zhang, G. Zeng, L. Niu, Y. Ling, Y. Zhang, Facile construction of 2D g-C₃N₄ supported nanoflower-like NaBiO₃ with direct Z-scheme heterojunctions and insight into its photocatalytic degradation of tetracycline, *J. Hazard. Mater.* 414 (2021), 125547.
- [5] C. Lops, A. Ancona, K. Di Cesare, B. Dumontel, N. Garino, G. Canavese, S. Hernández, V. Cauda, Sonophotocatalytic degradation mechanisms of Rhodamine B dye via radicals generation by micro- and nano-particles of ZnO, *Appl. Catal. B* 243 (2019) 629–640.
- [6] A. Afzal, P. Drzewicz, L.A. Pérez-Estrada, Y. Chen, J.W. Martin, M. Gamal El-Din, Effect of molecular structure on the relative reactivity of naphthenic acids in the UV/H₂O₂ advanced oxidation process, *Environ. Sci. Eng.* 46 (2012) 10727–10734.
- [7] Y. Yang, G. Zeng, D. Huang, C. Zhang, D. He, C. Zhou, W. Wang, W. Xiong, X. Li, B. Li, W. Dong, Y. Zhou, Molecular engineering of polymeric carbon nitride for highly efficient photocatalytic oxytetracycline degradation and H₂O₂ production, *Appl. Catal. B* 272 (2020), 118970.
- [8] C. Feng, L. Tang, Y. Deng, J. Wang, Y. Liu, X. Ouyang, H. Yang, J. Yu, J. Wang, A novel sulfur-assisted annealing method of g-C₃N₄ nanosheet compensates for the loss of light absorption with further promoted charge transfer for photocatalytic production of H₂ and H₂O₂, *Appl. Catal. B* 281 (2021), 119539.
- [9] W. Chen, Z.-C. He, G.-B. Huang, C.-L. Wu, W.-F. Chen, X.-H. Liu, Direct Z-scheme 2D/2D MnIn₂S₄/g-C₃N₄ architectures with highly efficient photocatalytic activities towards treatment of pharmaceutical wastewater and hydrogen evolution, *Chem. Eng. J.* 359 (2019) 244–253.
- [10] J. Yi, T. Fei, L. Li, Q. Yu, S. Zhang, Y. Song, J. Lian, X. Zhu, J. Deng, H. Xu, H. Li, Large-scale production of ultrathin carbon nitride-based photocatalysts for high-yield hydrogen evolution, *Appl. Catal. B* 281 (2021), 119475.
- [11] M. Jourshabani, B.-K. Lee, Z. Shariatinia, From traditional strategies to Z-scheme configuration in graphitic carbon nitride photocatalysts: recent progress and future challenges, *Appl. Catal. B* 276 (2020), 119157.
- [12] S. Wang, Y. Liu, J. Wang, Peroxymonosulfate activation by Fe–Co–O-codoped graphite carbon nitride for degradation of sulfamethoxazole, *Environ. Sci. Technol.* 54 (2020) 10361–10369.
- [13] T. Jordan, N. Fechner, J. Xu, T.J. Brenner, M. Antonietti, M. Shalom, “Caffeine doping” of carbon/nitrogen-based organic catalysts: Caffeine as a supramolecular edge modifier for the synthesis of photoactive carbon nitride tubes, *ChemCatChem* 7 (2015) 2826–2830.
- [14] M. Shalom, S. Inal, C. Fetzkenhauer, D. Neher, M. Antonietti, Improving carbon nitride photocatalysis by supramolecular preorganization of monomers, *J. Am. Chem. Soc.* 135 (2013) 7118–7121.
- [15] J. Barrio, M. Shalom, Rational design of carbon nitride materials by supramolecular preorganization of monomers, *ChemCatChem* 10 (2018) 5573–5586.
- [16] G. Liu, P. Niu, C. Sun, S.C. Smith, Z. Chen, G.Q. Lu, H.-M. Cheng, Unique electronic structure induced high photoreactivity of sulfur-doped graphitic C₃N₄, *J. Am. Chem. Soc.* 132 (2010) 11642–11648.
- [17] J. Li, B. Shen, Z. Hong, B. Lin, B. Gao, Y. Chen, A facile approach to synthesize novel oxygen-doped g-C₃N₄ with superior visible-light photoreactivity, *Chem. Commun.* 48 (2012) 12017–12019.
- [18] M. Jourshabani, Z. Shariatinia, G. Achari, C.H. Langford, A. Badiei, Facile synthesis of NiS₂ nanoparticles ingrafted in a sulfur-doped carbon nitride framework with enhanced visible light photocatalytic activity: two functional roles of thiourea, *J. Mater. Chem.* 6 (2018) 13448–13466.
- [19] F. Mayr, R. Brimiouille, T. Bach, A. Chiral, Thiourea as a Template for Enantioselective Intramolecular [2 + 2] Photocycloaddition Reactions, *J. Org. Chem.* 81 (2016) 6965–6971.
- [20] S. Guo, Z. Deng, M. Li, B. Jiang, C. Tian, Q. Pan, H. Fu, Phosphorus-doped carbon nitride tubes with a layered micro-nanostructure for enhanced visible-light photocatalytic hydrogen evolution, *Angew. Chem., Int. Ed.* 55 (2016) 1830–1834.
- [21] B.R. Bhogala, B. Captain, A. Parthasarathy, V. Ramamurthy, Thiourea as a template for photodimerization of azastilbenes, *J. Am. Chem. Soc.* 132 (2010) 13434–13442.
- [22] B. Lindberg, I.K. Hamrin, G. Johansson, U. Gelius, A. Fahlman, C. Nordling, K. Siegbahn, Molecular spectroscopy by means of ESCA II. Sulfur compounds. Correlation of electron binding energy with structure, *Phys. Scr.* 1 (1970) 286–298.
- [23] A. Yamaguchi, R. Penland, S. Mizushima, T. Lane, C. Curran, J. Quagliano, Infrared absorption spectra of inorganic coordination complexes. XIV. Infrared studies of some metal thiourea complexes, *J. Am. Chem. Soc.* 80 (1958) 527–529.
- [24] Y. Cui, J. Zhang, G. Zhang, J. Huang, P. Liu, M. Antonietti, X. Wang, Synthesis of bulk and nanoporous carbon nitride polymers from ammonium thiocyanate for photocatalytic hydrogen evolution, *J. Mater. Chem.* 21 (2011) 13032–13039.
- [25] A. Thomas, A. Fischer, F. Goettmann, M. Antonietti, J.-O. Müller, R. Schlögl, J. M. Carlsson, Graphitic carbon nitride materials: variation of structure and morphology and their use as metal-free catalysts, *J. Mater. Chem.* 18 (2008) 4893–4908.
- [26] J. Zhang, B. Xin, C. Shan, W. Zhang, D.D. Dionysiou, B. Pan, Roles of oxygen-containing functional groups of O-doped g-C₃N₄ in catalytic ozonation: Quantitative relationship and first-principles investigation, *Appl. Catal. B* 292 (2021), 120155.
- [27] R. Shen, K. He, A. Zhang, N. Li, Y.H. Ng, P. Zhang, J. Hu, X. Li, In-situ construction of metallic Ni₃C@Ni core-shell cocatalysts over g-C₃N₄ nanosheets for shell-thickness-dependent photocatalytic H₂ production, *Appl. Catal. B* 291 (2021), 120104.
- [28] K.-Y.A. Lin, Z.-Y. Zhang, Metal-free activation of Oxone using one-step prepared sulfur-doped carbon nitride under visible light irradiation, *Sep. Purif. Technol.* 173 (2017) 72–79.
- [29] K. Wang, Q. Li, B. Liu, B. Cheng, W. Ho, J. Yu, Sulfur-doped g-C₃N₄ with enhanced photocatalytic CO₂-reduction performance, *Appl. Catal. B* 176–177 (2015) 44–52.
- [30] Q. Liu, C. Chen, K. Yuan, C.D. Sewell, Z. Zhang, X. Fang, Z. Lin, Robust route to highly porous graphitic carbon nitride microtubes with preferred adsorption ability via rational design of one-dimension supramolecular precursors for efficient photocatalytic CO₂ conversion, *Nano Energy* 77 (2020), 105104.
- [31] T. Song, L. Hou, B. Long, A. Ali, G.-J. Deng, Constructing ultralong hollow chain-ball-like carbon nitride implanted with oxygen for superior visible-light photocatalytic hydrogen production, *J. Alloy. Compd.* 857 (2020), 157609.
- [32] X. Zong, L. Niu, W. Jiang, Y. Yu, L. An, D. Qu, X. Wang, Z. Sun, Constructing creatinine-derived moiety as donor block for carbon nitride photocatalyst with extended absorption and spatial charge separation, *Appl. Catal. B* 291 (2021), 120099.
- [33] Z. Wang, W. Guan, Y. Sun, F. Dong, Y. Zhou, W.-K. Ho, Water-assisted production of honeycomb-like g-C₃N₄ with ultralong carrier lifetime and outstanding photocatalytic activity, *Nanoscale* 7 (2015) 2471–2479.
- [34] M. Jourshabani, Z. Shariatinia, A. Badiei, Controllable synthesis of mesoporous sulfur-doped carbon nitride materials for enhanced visible light photocatalytic degradation, *Langmuir* 33 (2017) 7062–7078.
- [35] L. Jiang, X. Yuan, Y. Pan, J. Liang, G. Zeng, Z. Wu, H. Wang, Doping of graphitic carbon nitride for photocatalysis: A review, *Appl. Catal. B* 217 (2017) 388–406.
- [36] M. Chen, R. Bai, P. Jin, J. Li, Y. Yan, A. Peng, J. He, A facile hydrothermal synthesis of few-layer oxygen-doped g-C₃N₄ with enhanced visible light-responsive photocatalytic activity, *J. Alloy. Compd.* 869 (2021), 159292.
- [37] J. Huang, B. Wang, Z. Hao, Z. Zhou, Y. Qu, Boosting charge separation and broadening NIR light response over defected WO₃ quantum dots coupled g-C₃N₄ nanosheets for photocatalytic degrading antibiotics, *Chem. Eng. J.* 416 (2021), 129109.
- [38] Y. Zhang, T. Mori, J. Ye, M. Antonietti, Phosphorus-doped carbon nitride solid: enhanced electrical conductivity and photocurrent generation, *J. Am. Chem. Soc.* 132 (2010) 6294–6295.
- [39] J. Ran, T.Y. Ma, G. Gao, X.-W. Du, S.Z. Qiao, Porous P-doped graphitic carbon nitride nanosheets for synergistically enhanced visible-light photocatalytic H₂ production, *Energy Environ. Sci.* 8 (2015) 3708–3717.
- [40] J. Xu, Q. Gao, Z. Wang, Y. Zhu, An all-organic 0D/2D supramolecular porphyrin/g-C₃N₄ heterojunction assembled via π - π interaction for efficient visible photocatalytic oxidation, *Appl. Catal. B* 291 (2021), 120059.
- [41] J. Kelly, D. Vanmaekelbergh, Charge carrier dynamics in nanoporous photoelectrodes, *Electrochim. Acta* 43 (1998) 2773–2780.
- [42] Y.-X. Ye, C. Wen, J. Pan, J.-W. Wang, Y.-J. Tong, S. Wei, Z. Ke, L. Jiang, F. Zhu, N. Zhou, M. Zhou, J. Xu, G. Ouyang, Visible-light driven efficient overall H₂O₂ production on modified graphitic carbon nitride under ambient conditions, *Appl. Catal. B* 285 (2021), 119726.
- [43] G. Di, Z. Zhu, H. Zhang, J. Zhu, Y. Qiu, D. Yin, S. Küppers, Visible-light degradation of sulfonamides by Z-scheme ZnO/g-C₃N₄ heterojunctions with amorphous Fe₂O₃ as electron mediator, *J. Colloid Interface Sci.* 538 (2019) 256–266.
- [44] C. Zhao, F. Ran, L. Dai, C. Li, C. Zheng, C. Si, Cellulose-assisted construction of high surface area Z-scheme C-doped g-C₃N₄/WO₃ for improved tetracycline degradation, *Carbohydr. Polym.* 255 (2020), 117343.
- [45] Z. Mo, H. Xu, Z. Chen, X. She, Y. Song, J. Lian, X. Zhu, P. Yan, Y. Lei, S. Yuan, H. Li, Construction of MnO₂/monolayer g-C₃N₄ with Mn vacancies for Z-scheme overall water splitting, *Appl. Catal. B* 241 (2019) 452–460.